



## Article

# Assessing the Spatial–Temporal Pattern of Spring Maize Drought in Northeast China Using an Optimised Remote Sensing Index

Yihao Wang <sup>1,2</sup> , Yongfeng Wu <sup>1,\*</sup>, Lin Ji <sup>1</sup>, Jinshui Zhang <sup>3</sup> and Linghua Meng <sup>2</sup>

- <sup>1</sup> Institute of Agricultural Environment and Sustainable Development, Chinese Academy of Agricultural Sciences, Beijing 100081, China; wangyihao@iga.ac.cn (Y.W.); jilin@caas.cn (L.J.)
- <sup>2</sup> Northeast Institute of Geography and Agroecology, Chinese Academy of Sciences, Changchun 130102, China; menglinghua@iga.ac.cn
- <sup>3</sup> Beijing Land Surface Remote Sensing Data Product Engineering Technology Research Center, Department of Geography, Beijing Normal University, Beijing 100081, China; zhangjs@bnu.edu.cn
- \* Correspondence: wuyongfeng@caas.cn

**Abstract:** Northeast China plays a pivotal role in producing commodity grains. The precipitation and temperature distribution during the growth season is impacted by geographical and climate factors, rendering the region vulnerable to drought. However, relying on a single index does not reflect the severity and extent of drought in different regions. This research utilised the random forest (RF) model for screening remote sensing indices. Relative soil moisture (RSM) was employed to compare seven commonly used indices: the temperature vegetation dryness index (TVDI), vegetation supply water index (VSWI), vegetation condition index (VCI), temperature condition index (TCI), vegetation health index (VHI), multi-band drought index (MBDI), and normalised difference drought index (NDDI). The effectiveness of these indices for monitoring drought during different developmental stages of spring maize was evaluated. Trend rates were employed to investigate the temporal changes in drought patterns of spring maize from 2003 to 2020, and the Sen + Mann–Kendall test was used to analyse spatial variations. The results showed the following: (1) The seven remote sensing indices could accurately track drought during critical growth stages with the TVDI demonstrating higher applicability than the other six indices. (2) The application periods of two TVDIs with different parameters differed for the drought monitoring of spring maize in different developmental periods. The consistency and accuracy of the normalised difference vegetation index (NDVI)-based TVDI (TVDI<sub>N</sub>) were 5.77% and 34.62% higher than those of the enhanced vegetation index (EVI)-based TVDI (TVDI<sub>E</sub>), respectively, in the early stage. In contrast, the TVDI<sub>E</sub> exhibited 13.46% higher consistency than the TVDI<sub>N</sub> in the middle stage, and the accuracy was the same. During the later stage, the TVDI<sub>E</sub> showed significantly higher consistency and accuracy than the TVDI<sub>N</sub> with consistency increases of 9.61% and 38.64%, respectively. (3) The drought trend in northeast China increased from 2003 to 2020, exhibiting severe spring drought and a weakening of the drought in summer. The southern, southwestern, and northwestern parts of northeast China showed an upward drought trend; the drought-affected areas accounted for 37.91% of the study area. This paper identified the most suitable remote sensing indices for monitoring drought in different developmental stages of spring maize. The results provide a comprehensive understanding of the spatial–temporal patterns of drought during the past 18 years. These findings can be used to develop a dynamic agricultural drought monitoring model to ensure food security.



**Citation:** Wang, Y.; Wu, Y.; Ji, L.; Zhang, J.; Meng, L. Assessing the Spatial–Temporal Pattern of Spring Maize Drought in Northeast China Using an Optimised Remote Sensing Index. *Remote Sens.* **2023**, *15*, 4171. <https://doi.org/10.3390/rs15174171>

Academic Editors: Dongryeol Ryu, Hao Sun and Liangliang Tao

Received: 5 July 2023

Revised: 15 August 2023

Accepted: 19 August 2023

Published: 25 August 2023



**Copyright:** © 2023 by the authors. Licensee MDPI, Basel, Switzerland. This article is an open access article distributed under the terms and conditions of the Creative Commons Attribution (CC BY) license (<https://creativecommons.org/licenses/by/4.0/>).

**Keywords:** northeast China; spring maize; spatial-temporal pattern; drought monitoring; random forest model; Sen + Mann–Kendall test model

## 1. Introduction

Drought has significant impacts on crop growth, causing fluctuations in food prices and triggering global food crises [1,2]. The impact of drought is also severe in China, with an average annual affected area and disaster area of  $2.1 \times 10^7$  hm<sup>2</sup> and  $8.9 \times 10^6$  hm<sup>2</sup>, respectively [3]. Moreover, the average annual direct economic loss is 44 billion CNY [4]. The drought pattern has changed due to global climate warming, worsening the situation in northeast China [5]. Northeast China is situated in the ‘golden corn belt’ [6], with a corn planting area of  $6 \times 10^6 \sim 7 \times 10^6$  hm<sup>2</sup> and an annual output of over  $4 \times 10^9$  t, accounting for 33% of the total national corn output [7]. Despite the increase in production input and advancements in science and technology, the planting area and yield of spring maize remain vulnerable to the effects of drought [8]. The region is characterised by rain-fed agriculture. The anomalous atmospheric circulation caused by the East Asian tropical monsoon and the subtropical monsoon has resulted in decreased precipitation during crop growth seasons in recent years [9]. This frequent occurrence of drought during the spring maize growth season highlights the importance of obtaining better insights into the patterns of drought occurrence, development, and recession as well as accurately identifying the spatial–temporal patterns of drought under the background of climate change [10,11]. Doing so will enable us to take appropriate disaster prevention measures, adjust planting schedules, ensure the healthy and stable development of the agricultural economy, and achieve stable grain yields. Thus, this research is critical for northeast China [12].

Current drought monitoring primarily relies on two data sources: meteorological observation stations and satellite remote sensing [13–15]. However, meteorological stations are unevenly distributed, making it difficult to carry out high-precision drought monitoring in areas with sparse stations [15,16]. Additionally, drought monitoring based solely on meteorological data does not account for the water requirements of vegetation or the water status of the soil, leading to limitations in agricultural drought monitoring [17]. Due to the advancement of remote sensing technology, remote sensing data have become more reliable for monitoring large-scale spatial–temporal patterns of drought [18]. Remote sensing data offer wide coverage, high spatial resolution, and timeliness, providing information on crop growth and canopy cover before and after disasters [19].

Remote sensing-based drought monitoring methods fall into four categories. The first category is the vegetation index (VI) method, which links vegetation growth status with drought. This method is widely used, and the most commonly used VIs include the normalised difference vegetation index (NDVI) proposed by Tucker [20], the vegetation condition index (VCI) proposed by Kogan [21], and the enhanced vegetation index (EVI) proposed by Liu and Huete [22]. These indices reflect the photosynthetic activity, canopy structure, and vegetation cover of crops, providing valuable information for monitoring drought conditions. However, the VI method has some limitations, including sensitivity to atmospheric conditions, soil background interference, and saturation under high biomass conditions. The second category is the combined use of VIs and land surface temperature (LST). Commonly used VIs include the vegetation health index (VHI) proposed by Kogan [23], the vegetation and soil moisture index (VSWI) proposed by Carlson [24], and the temperature vegetation dryness index (TVDI) proposed by Sandholt [25]. This method combines the advantages of VIs and LST in drought monitoring and has been widely used in identifying drought and its spatial–temporal patterns [26]. However, these indices are more suitable for the entire vegetation coverage period, and they are based on statistical analysis; thus, they may not accurately reflect drought conditions. The third category is based on the surface energy balance theory, which focuses on the soil. Common indices used in this method include the crop water stress index (CWSI) proposed by Idso [27] and the water deficit index (WDI) proposed by Moran [28]. However, this method is only applicable to periods of bare soil or low vegetation coverage. Additionally, the temperature obtained from remote sensing images may have substantial uncertainty, limiting the accuracy of this method for drought monitoring [29]. The fourth category is active and passive microwave remote sensing. This method has been widely used in soil moisture inversion because

the data acquisition is not affected by atmospheric conditions [30]. Although microwave remote sensing is very sensitive to soil moisture, its spatial resolution is often coarse, and the accuracy of drought identification may not be as high as that of other remote sensing methods [31].

Due to the complexity of the earth–atmosphere system, the diversity of organisms, and drought variability, the applicability and accuracy of remote sensing indices for drought monitoring may be affected by many factors, such as time and space, farmland environment, crop type, and different developmental stages of crops [32]. Previous studies have indicated that remote sensing indices vary significantly in different regions, and a single index may not reflect the intensity and severity of drought in different regions [33–35]. Therefore, it is necessary to evaluate the accuracy and applicability of a drought index before use. Researchers have improved and revised common remote sensing indices by considering the influence of the farmland environment and regional climate factors in different research areas and for different research objects and purposes to improve the accuracy of drought monitoring. The improved remote sensing indices better reflect the drought conditions of local crops [36–38]. Some scholars have observed differences in the sensitive period of remote sensing indices when the indices were constructed with different parameters [39,40]. Additionally, the correlation difference between the moisture content of the cultivated soil layer and remote sensing indices has been used to evaluate the applicability of remote sensing indicators to assess agricultural drought and the limitation of their spatial–temporal application range. Some researchers are also exploring the applicability of remote sensing indices based on deep learning algorithms, such as the random forest (RF) model and convolutional neural networks [41,42]. These studies provide a theoretical basis for improving the accuracy of drought monitoring and determining the sensitive periods of remote sensing indices constructed with different parameters in northeast China [29].

Drought remote sensing monitoring has a wide range of applications, but drought characteristics differ in different regions and for different crops [23]. It is crucial to ensure that the selected indicators are applicable to drought monitoring [13,14]. Most research on drought monitoring in northeast China utilised meteorological data to evaluate the intensity, affected area, and spatial–temporal patterns of drought. However, a lack of research exists on the applicability of drought monitoring indices and the spatial–temporal patterns of drought using remote sensing data against the background of climate change. Therefore, this study has two objectives: (1) to evaluate seven widely used drought indices (TVDI, TCI, VCI, MBDI, VHI, NDDI and VSWI) and determine the best index for drought monitoring in the study area and (2) to explore the spatial–temporal patterns of drought in the study area from 2003 to 2020.

## 2. Material and Methods

### 2.1. Study Area

The study area covers a total area of approximately  $14,500 \times 10^4$  hm<sup>2</sup> and is located between 38°72′–53°56′N and 115°52′–135°09′E, including Liaoning, Jilin, Heilongjiang, and eastern Inner Mongolia. The main crop in this area is spring maize, which is followed by soybean and rice [43]. Due to the high cumulative temperature, only one crop per year is possible for spring maize in northeast China [8]. The study area and the spring maize planting area are shown in Figure 1a. The area is characterised by high altitudes in the northwest and southeast with a dominant presence of forestland [9]. The central and eastern terrain is flat; therefore, these are the main planting areas for spring maize. The southeast receives more rainfall than the northwest due to geographical and climatic factors. The spatial–temporal distributions of temperature and precipitation in the spring maize area are uneven with low rainfall occurring in May and high temperatures in July despite abundant precipitation (Figure 1b,c) [11,12]. Therefore, the region is prone to large-scale drought before and after the seedling and kernel-filling periods, significantly affecting the growth and development of spring maize. The average temperature ( $T_{\text{mean}}$ ) during the

growing season has shown an increasing trend, whereas the cumulative precipitation (PRE) has shown a decreasing trend in the past 36 years (Figure 1d) [43,44].

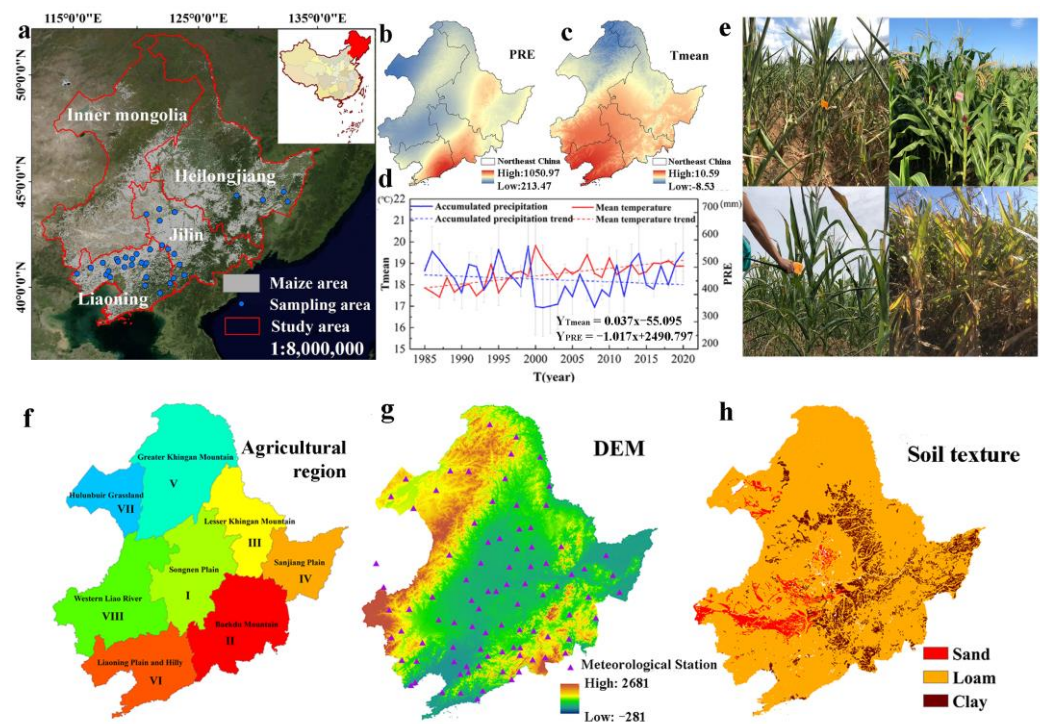


**Figure 1.** The study area in northeast China: (a) spring maize area and sampling areas in 2018, (b,c) multiyear PRE and Tmean, (d) Tmean and PRE trend in the growing season from 1985 to 2020, (e) drought investigation of spring maize, (f) agricultural regions. Note: I, Songnen Plain Zone; II, Baekdu Mountain Zone; III, Lesser Khingan Mountain Zone; IV, Sanjiang Plain Zone; V Greater Khingan Mountain Zone; VI, Liaoning Plain and Hilly Zone; VII, Hulunbuir Grassland Zone; VIII, Western Liao River Zone. (g) DEM and meteorological stations, and (h) soil texture.

## 2.2. Data Sources and Data Processing

### 2.2.1. NDVI, EVI, and LST Time-Series Data

The MOD09A1 (8-d surface reflectance (SR); 500 m resolution) and MOD11A2 (8-d LST; 1000 m resolution) data products were downloaded from Google Earth Engine (GEE) (<https://code.earthengine.google.com>) (accessed on 3 July 2023). The NDVI and EVI were calculated based on the SR data using the ENVI + IDL programming environment. Some values were missing due to clouds and shadows. Therefore, linear interpolation was used to fill the missing values [45,46]. Additionally, Savitzky–Golay filtering was applied to denoise the data. Second, a local regression model of NDVI and LST was used to interpolate the missing LST values to obtain spatially continuous LST data. Finally, the spatial–temporal resolutions of the remote sensing data used in this study were standardised to 8 d and 1000 m, respectively.

### 2.2.2. Spring Maize Area

Sentinel-2 SR products from April to August 2018 covering Northeast China were selected in GEE (<https://code.earthengine.google.com>) (accessed on 3 July 2023). After cloud removal and shadow processing, the missing values were replaced by data from cloudless images from 2017 or 2016 to obtain a composite image covering the study area. The NDVI and NDWI of the synthetic images from April to July were calculated, and the seven bands (coastal aerosol, blue, green, red, near-infrared, shortwave infrared 1, and shortwave infrared 2) of the synthetic images from August were used as the prediction bands of the RF classifier. The RF classifier consisted of 20 trees, and 4900 sample points in

seven categories (water, town, forest land, maize, rice, soybean, and unused land) were used to train the classifier in GEE. The image was classified into seven categories, and the maize areas were extracted. The classification accuracy of the spring maize area was calculated using 194 spring maize points identified and recorded by handheld GPS during three field surveys in 2018. The final classification accuracy was 87.1% [45]. This study focused on the applicability of drought monitoring indicators and the spatio-temporal pattern of drought in spring maize areas under the background of climate change. Since the field survey data for the accuracy assessments were collected in 2018, the spring maize area in 2018 was used as the base map of the multiyear distribution of spring maize in northeast China.

### 2.2.3. Relative Soil Moisture Data

The relative soil moisture (RSM) data came from the China Land Data Assimilation System (CLDAS) V2.0 dataset of the China Meteorological Data Network (<http://data.cma.cn>) (accessed on 3 July 2023). The daily RSM<sub>10</sub> and RSM<sub>20</sub> data of the spring maize growing season in 2017 and 2018 were used as basic data. We used Python 3.7 to convert the NC format into the TIFF format to construct a geographically weighted regression model [47] of RSM, NDVI, and LST data. The 5 km resolution RSM data were resampled to 1000 m. The average RSM value of 8 d in the same period as the remote sensing data was calculated and recorded as the RSM value of the period, creating RSM data consistent with the spatial–temporal resolution of the remote sensing data. The RSM was used as the dependent variable, and the remote sensing indices were the independent variables in the RF model, which was used to select the optimal remote sensing index.

### 2.2.4. Validation Data

The validation data were obtained from a real-time survey of spring maize areas in 2018. The survey data included surface soil and plant drought data. The research group collected surface soil samples before and after the emergence of spring maize from May 14th to 18th, before and after the spring maize big trumpet period between July 12th and 19th (the middle stage of spring maize growth), and before and after the filling period from August 6th to 14th (the final stage of spring maize growth). The locations of the sample sites were recorded with handheld GPS devices. A total of 52 soil samples were collected (Figure 1a), and drought symptoms were recorded (Figure 1c) Soil samples in four soil layers (5 cm per layer) were obtained at each sample location. The drought status of spring maize was documented via photography, and the RSM was determined by laboratory analysis. The survey area for the drought that impacted spring maize in 2018 is shown in Figure 1a. It covered a large area of spring maize planting locations on different slopes, at different altitudes, and in soils with different textures. The survey covered every critical developmental phase from pre-emergence to the filling stage of maize; thus, the data are highly representative, ensuring the credibility and accuracy of the research findings.

### 2.2.5. Other Data

We used soil texture data and a digital elevation model (DEM) obtained from the Resource and Environmental Science Data Centre of the Chinese Academy of Sciences (<http://www.resdc.cn>) (accessed on 3 July 2023). We used 1 km resolution soil texture data to discern sandy, clay, and loam soil. The 30 m resolution DEM data were employed to extract terrain factors. ArcGIS 10.2 was used to extract and process the pertinent information from the data, enhancing the accuracy and precision of the results.

## 2.3. Method

### 2.3.1. Selection of Remote Sensing Indices

Following studies on the remote sensing monitoring of agricultural drought [19,27,32,33], seven widely used remote sensing indices were selected. These indexes were calculated

using the MOD09A1 and MOD11A2 products. The VI equations and descriptions are listed in Table 1.

**Table 1.** Vegetation index type and equations.

Remote Sensing Index	Formula	Index Type	Reference
TVDI	$TVDI = \frac{LST_{VIi} - LST_{VIimin}}{LST_{VIimax} - LST_{VIimin}}$ $LST_{VIimax} = a_1 + b_1 VIi$ $LST_{VIimin} = a_2 + b_2 VIi$	Vegetation Index Canopy Temperature	Sandholt et al. (2002) [25]
VSWI	$VSWI = \frac{NDVI}{LST}$	Vegetation Index Canopy Temperature	Carlson et al. (1994) [24]
VCI	$VCI = \frac{NDVI - NDVI_{min}}{NDVI_{max} - NDVI_{min}}$	Vegetation Index	Kogan (1990) [21]
TCI	$TCI = \frac{LST_{max} - LST}{LST_{max} - LST_{min}}$	Canopy Temperature	Tja et al. (2020) [48]
VHI	$VHI = a \times VCI + (1 - a) \times TCI$	Vegetation Index Canopy Temperature	Kogan (1995) [23]
MBDI	$MBDI = \frac{NDWI}{LST}$	Canopy Water Content Canopy Temperature	Li et al. (2022) [36]
NDDI	$NDDI = \frac{NDVI - NDWI}{NDVI + NDWI}$	Vegetation Index Canopy Water Content	Trisasongko et al. (2015) [37]

### 2.3.2. Selection of the Optimal Remote Sensing Index and Parameter Optimisation

This study employed the RF package in the R language to establish the RF model and select the optimal remote sensing index [38]. An RM model consists of multiple decision trees. Each tree randomly selected 80% of the training samples to construct a decision tree. The remaining 20% of the data was the out-of-bag sample, which was used as the test set to compute the out-of-bag error. Assessing this error is similar to performing cross-validation; thus, there is no need for cross-validation. The RF model had three crucial parameters: the number of decision trees (ntree), the number of random variables for splitting nodes (mtry), and the importance of the independent variables. Based on the initial experimental results, we used 500 ntree and 1/3 of the mtry as inputs into the RF model. The importance parameter was set to True.

The model outputs the importance values of the independent variables, based on which we calculated the weights of the independent variables using Equation (1). The higher the weight, the greater the response of the independent variable to the change in the RSM, and the stronger the correlation between the independent variable and the RSM.

$$P_a = \frac{Q_a}{\sum_{i=1}^n Q_i} \quad (1)$$

where  $P_a$  is the weight of the index;  $Q_i$  ( $i = 1, 2, 3, \dots, n$ ) is the importance value of each index, and  $Q_a$  ( $a = 1, 2, 3, \dots, n$ ) is the sum of the important values of all indicators. The value of  $i$  is 7 in this study.

The screening and optimisation steps were as follows.

- (1) Wen [49] observed that the roots with high water absorption capacity of spring maize during the seedling stage were primarily located at a depth of 10 cm. Consequently, we established two RF models for different stages of spring maize growth: one for the seedling stage and another for the remaining period. We used the seven remote sensing indices as independent variables in both models. The dependent variables were  $RSM_{10}$  and  $RSM_{20}$  for soil depths of 10 cm and 20 cm, respectively.
- (2) The RF model was utilised to ascertain the importance of the remote sensing indices in responding to changes in the RSM at various developmental stages of spring maize. The weighting factor  $P$  (Equation (1)) was determined, and the index weights during

different developmental phases of spring maize were analysed to assess which indices were the most suitable for different developmental stages of spring maize.

- (3) When the construction parameter of the optimal remote sensing index contains VI, we will calculate the optimal remote sensing index constructed by different VIs. The optimal remote sensing index in different developmental phases of spring maize was determined by comparing the coefficient of determination ( $R^2$ ) of the regression between the optimal remote sensing index and the RSM. The calculation steps were performed in the ENVI + IDL programming environment.
- (4) The optimal remote sensing index was used to analyse the spatial–temporal patterns of spring maize drought in northeast China from 2003 to 2020.

The flowchart for determining the optimal vegetation index is shown in Figure 2.

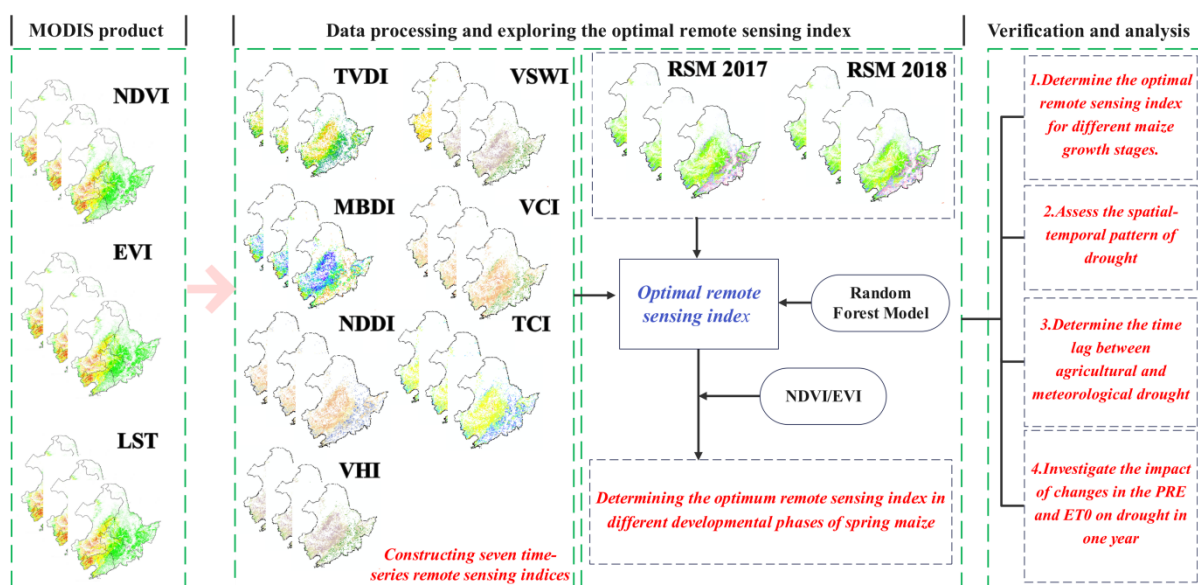


**Figure 2.** Flowchart for determining the optimal vegetation index.

### 2.3.3. Drought Levels and Validation

The drought levels of spring maize during different periods were based on the standard ‘Northern China spring maize drought levels’ (QX/T 259-2015), which is a meteorological industry standard. The drought level was assessed before and after the emergence of spring maize; the underlying surface type developed from a single surface (completely bare soil coverage) to a mixed surface. It was determined using the field-measure RSM. The drought level was ascertained using  $RSM_{10}$  for different soil textures during the emergence–jointing periods. The soil had vegetation cover during the kernel–filling period, and the drought level was characterised by the drought symptoms of the maize plants and not the RSM of the topsoil. The morphological characteristics of the maize plants were recorded, and the drought level in the tasseling–milk periods was determined by the meteorological industry standard.

Drought consistency and accuracy were used for model validation. The accuracy validation method proposed by Ma [50] was used to verify the model for each developmental stage of spring maize. The equation is as follows.

$$POD = \frac{H}{H + M} \times 100\% \quad (2)$$

where  $POD$  is the accuracy;  $H$  is the number of sample areas whose drought level is correctly identified; and  $M$  is the number of sample areas whose drought level is incorrectly identified.

### 2.3.4. Evaluation of the Multiyear Drought Trend in the Spring Maize Area of Northeast China

Regression analysis [51] was used to evaluate the time trend of multiyear drought based on the optimal remote sensing index in different development stages of spring maize. The slope of the dry edge was selected to analyse the 8-day LST-VI feature space of the key development period of spring maize from 2003 to 2020. The equation is as follows:

$$e_{slope} = \frac{n \times \sum_{i=1}^n i \times \bar{X}_i - \sum_{i=1}^n i \times \sum_{j=1}^n \bar{X}_j}{n \times \sum_{i=1}^n i^2 - (\sum_{i=1}^n i)^2} \quad (3)$$

where  $i$  is the annual order, which represents the  $R^2$  of the dry–wet fitting equation in the LST-VI feature space of the  $i$ th year, and  $n$  represents the number of years. When  $e_{slope} > 0$ , the drought trend increases in  $n$  years and vice versa.

The Sen + Mann–Kendall test was used to evaluate the spatial trend of multiyear drought in the spring maize area of northeast China [52]. The Sen trend degree equation is defined as follows:

$$\beta = Median\left(\frac{x_j - x_i}{j - i}\right), \forall j > i \quad (4)$$

where  $1 < i < j < n$ ;  $Median()$  represents the median value. If  $\beta > 0$ , the drought exhibits an upward trend and vice versa. The Mann–Kendall test statistic  $S$  is calculated as follows:

$$S = \sum_{i=1}^{n-1} \sum_{j=i+1}^n sgn(x_j - x_i) \quad (5)$$

$$sgn(x_j - x_i) = \begin{cases} +1 & (x_j - x_i > 0) \\ 0 & (x_j - x_i = 0) \\ -1 & (x_j - x_i < 0) \end{cases} \quad (6)$$

Two test statistics are used for the trend test. The  $Z$  value is calculated as follows:

$$Z = \begin{cases} \frac{S-1}{\sqrt{VAR(S)}} & (S > 0) \\ 0 & (S = 0) \\ \frac{S+1}{\sqrt{VAR(S)}} & (S < 0) \end{cases} \quad (7)$$

$$VAR(S) = \frac{(n(n-1)(2n+5) - \sum_{i=1}^m t_i(t_i-1)(2t_i+5))}{18} \quad (8)$$

where  $n$  is the number of data points;  $m$  is the number of data groups that appear repeatedly; and  $t_i$  is the number of duplicate data points in group  $i$ . A bilateral trend test was performed on the  $Z$  value, and the critical value  $Z_{1-\alpha/2}$  was obtained from the distribution table at the given significance level. When  $|Z| \leq Z_{1-\alpha/2}$ , we accept the null hypothesis that the trend is not significant. Otherwise, we reject the null hypothesis and determine that the trend is significant. The critical value  $Z_{1-\alpha/2}$  is 1.65, 1.96, and 2.58, at confidence levels of 90%, 95%, and 99%, respectively. The trend analysis and mutation test were implemented in MATLAB 2016b. The interpretation of the Mann–Kendall test results is provided in Table 2.

The Mann–Kendall mutation test was selected to analyse the mutation time of the drought trend. When the UF and UB curves intersect, and the focus is the critical value ( $U_{0.05} = \pm 1.96$ ), the time corresponding to the intersection is the start time of the mutation.

**Table 2.** Interpretation of the Mann–Kendall test results.

$\beta$	Z	Trend Features
$\beta > 0$	$2.58 < Z$	Highly significant increase
	$1.96 < Z \leq 2.58$	Significant increase
	$1.65 < Z \leq 1.96$	Slightly significant increase
	$Z \leq 1.96$	Non-significant increase
$\beta = 0$	Z	No change
$\beta < 0$	$Z \leq 1.96$	Insignificant decrease
	$1.65 < Z \leq 1.96$	Slightly significant decrease
	$1.96 < Z \leq 2.58$	Significant decrease
	$2.58 < Z$	Highly significant decrease

### 2.3.5. Determination of Frequent Drought Periods in the Spring Maize Area of Northeast China

We used the Penman–Monteith equation recommended by FAO-56 to calculate the reference evapotranspiration (ET<sub>0</sub>) using precipitation, temperature, and sunshine hours in the past 36 years [53]. We determined the time difference between the precipitation and ET<sub>0</sub> in the study period to obtain the period of frequent droughts. The ET<sub>0</sub> is calculated as follows:

$$ET_0 = \frac{0.408 \cdot \Delta \cdot (R_n - G) + \gamma \cdot \frac{900}{T_{mean} + 273} \cdot U_2 \cdot (e_s - e_a)}{\Delta + \gamma \cdot (1 + 0.34 \cdot U_2)} \quad (9)$$

where  $R_n$  is the surface net radiation, MJ/(m<sup>2</sup>·d);  $g$  is the soil heat flux, MJ/(m<sup>2</sup>·d);  $T_{mean}$  is the average temperature, °C;  $U_2$  is the wind speed at the height of 2 m, m/s;  $e_s$  is the saturated water pressure,  $e_a$  is the actual water pressure, kPa;  $\delta$  is the slope of the saturated water pressure curve, kPa/°C; and  $\gamma$  is the surface constant, kPa/°C.

## 3. Result

### 3.1. Selecting the Optimal Remote Sensing Index

The remote sensing index weights for the RF model describing the relationship between RSM<sub>20</sub> and the indices during maize growth in 2017 and 2018 are shown in Figure 3a,b. The weight of TVDI is higher than the average weight (0.14) and that of the other indices during the development process of spring maize.

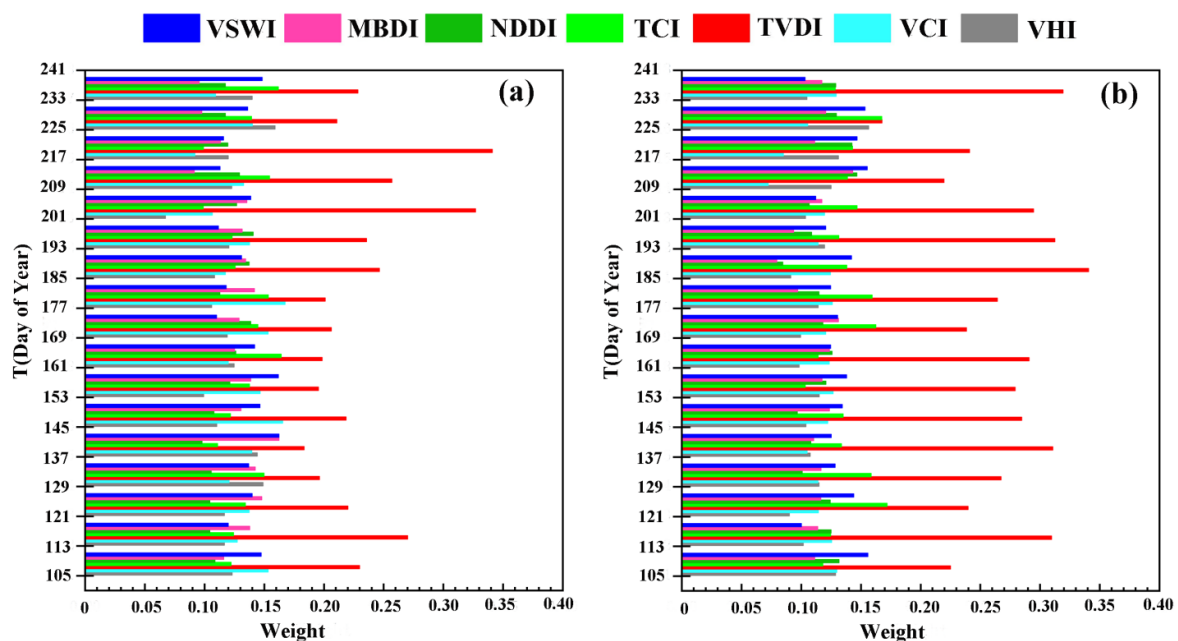


**Figure 3.** Remote sensing index weights for the RF model describing the relationship between RSM<sub>20</sub> and the indices during maize growth in (a) 2017 and (b) 2018.

### 3.2. Comparison of NDIV- and EVI-based TVDI

#### 3.2.1. Comparison of Drought Sensitivity of NDIV- and EVI-Based TVDI

Figure 4 shows the  $R^2$  of the NDIV-based TVDI ( $TVDI_N$ ) and EVI-based ( $TVDI_E$ ) in the key growth periods of spring maize in 2018. The  $R^2$  of  $TVDI_N$  was higher than that of  $TVDI_E$  in the early growth stage (emergence–jointing stage; day of year (DOY) 105–150). The maximum, minimum, and average differences in the  $R^2$  between the  $TVDI_N$  and  $TVDI_E$  were 0.44, 0.10, and 0.23, respectively. The fitting performance of the  $TVDI_N$  was significantly higher than that of the  $TVDI_E$ , making it more suitable for drought monitoring in this stage. The difference in the  $R^2$  between the  $TVDI_E$  and  $TVDI_N$  was 0.02–0.11 in the middle growth stage (jointing–kernel–filling stage, DOY 150–185). Therefore, this stage is regarded as the transition period. At the late growth stage (large bell-filling stage, DOY 185–240), the  $R^2$  of the  $TVDI_N$  was lower than that of the  $TVDI_E$ , and the maximum, minimum, and average differences in the  $R^2$  between the  $TVDI_E$  and  $TVDI_N$  were 0.29, 0.13, and 0.18, respectively. The fitting performance of the  $TVDI_E$  was significantly higher than that of the  $TVDI_N$ ; thus, it is more suitable for drought monitoring in this stage.

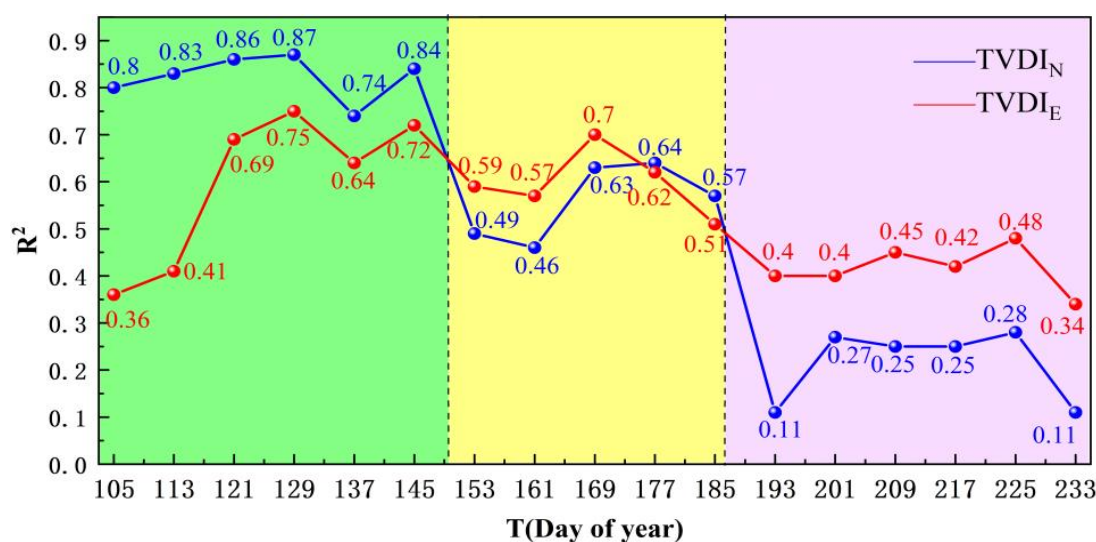


**Figure 4.** The  $R^2$  of the NDIV-based TVDI ( $TVDI_N$ ) and EVI-based TVDI ( $TVDI_E$ ) during maize growth.

#### 3.2.2. Comparison of TVDI Monitoring Accuracy in Different Farmland Environments

Table 3 shows the consistency and accuracy of the  $TVDI_N$  and  $TVDI_E$  in drought monitoring of the main planting areas of spring maize. The consistency and accuracy of the  $TVDI_E$  were 5.77% and 34.62% higher than those of  $TVDI_N$  in the seedling stage, respectively. The consistency of the  $TVDI_E$  was 13.46% higher than that of  $TVDI_N$ , and the accuracy was same in the kernel-filling stage. The consistency and accuracy of the  $TVDI_E$  were 9.61% and 38.46% higher than those of the  $TVDI_N$ , respectively, in the emergency period. The consistency (accuracy) of the  $TVDI_E$  was 5.08% and 11.53% (8.58% and 26.93%) higher, respectively, than that of the  $TVDI_E$  for slopes of 0–0.5° and 0.5–2.0°. The consistency and accuracy of the  $TVDI_E$  were 17.34% and 9.61% higher, respectively, than those of the  $TVDI_N$  for loamy soil. In contrast, the consistency was the same for the  $TVDI_N$  and  $TVDI_E$  for sandy soils, and the accuracy was 17.31% higher than that of the  $TVDI_N$ . The  $TVDI_E$  showed significantly higher consistency (7.69% and 1.92% higher) and accuracy (7.7% and 17.31% higher) than the  $TVDI_N$  at altitudes of 0–150 m and 150–300 m, respectively. The drought monitoring consistency and accuracy of the  $TVDI_E$  were higher than or equal to those of the  $TVDI_N$  in the seedling stage. Therefore, the  $TVDI_N$  is more suitable for drought monitoring in the early growth stage of spring maize, whereas the  $TVDI_E$  is more suitable for drought monitoring in the middle and late growth stages of spring maize. These results

can be used for selecting indices for drought monitoring in different development stages of spring maize, which will be addressed in a follow-up paper.

**Table 3.** Consistency and accuracy TVDI<sub>N</sub> and TVDI<sub>E</sub> for different farmland environments.

Item		Accuracy/%		Consistency/%	
		TVDI <sub>N</sub>	TVDI <sub>E</sub>	TVDI <sub>N</sub>	TVDI <sub>E</sub>
Developmental stage	Emergence	84.62	78.85	84.62	50.00
	Big flare	67.31	80.77	63.46	63.46
	Milk stage	73.08	82.69	40.39	78.85
Slope/°	0–0.5	69.20	75.00	50.00	61.53
	0.5–2.0	81.80	90.38	46.15	73.08
Soil texture	Loam	69.20	86.54	63.46	73.07
	Sand	67.31	67.31	50.00	67.31
Elevation/m	0–150	63.46	71.15	71.15	78.85
	150–300	84.62	86.54	50.00	67.31

### 3.3. Spatial–Temporal Pattern of Spring Maize Drought in Northeast China

#### 3.3.1. Temporal and Spatial Evolution Trend of Drought in the Study Area

Figure 5a,b shows the spatial–temporal evolution trends of drought in northeast China, respectively. The southern, southwestern, and northwestern parts of the study area showed an increasing drought trend in the key development stages of spring maize in the past 18 years. This area accounts for 37.91% of the total area of spring maize in northeast China (Figure 5a). The dry edge slope of the LST–VI feature space exhibited an upward trend, and the wet edge slope showed a downward trend (Figure 5b). This result indicated that the northeast region experienced more drought and less humidity during the past 18 years. The Mann–Kendall mutation test showed that the UF and UB curves of the TVDI mean time series intersected at approximately 2005, and the Z-score at the intersection point was  $\pm 1.96$  (Figure 5c). Thus, the mutation occurred in 2005, which was followed by an increasing trend ( $1.96 > Z > 0$ ), but the trend was not significant ( $Z > 1.96$ ).

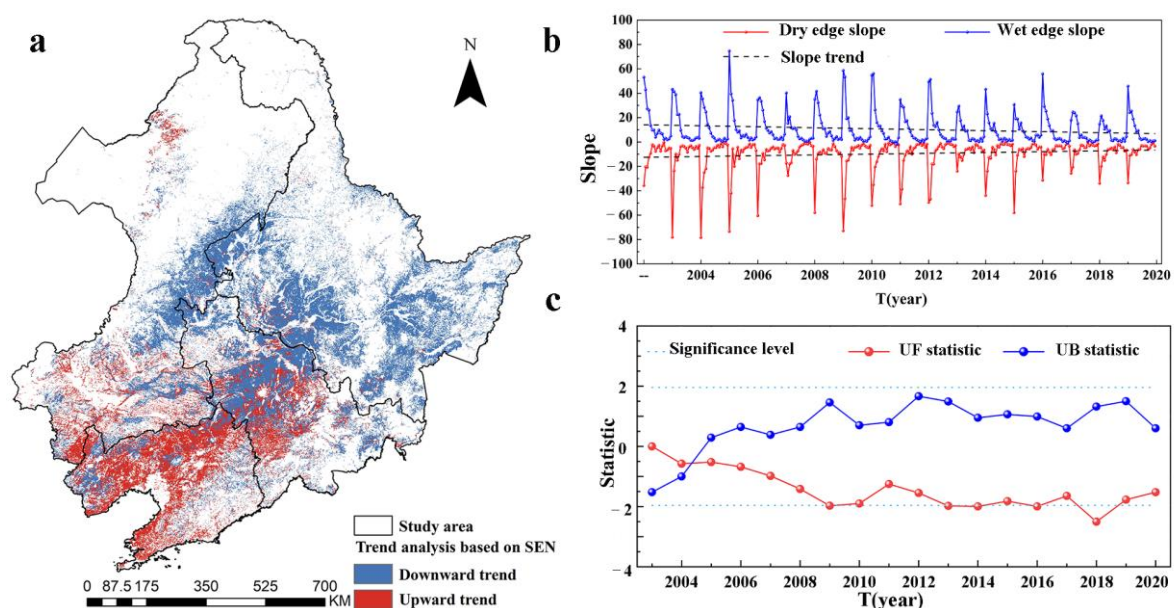


**Figure 5.** (a) Drought trend based on Sen's slope, (b) drying and wetting trends, and (c) MK test results.

### 3.3.2. Interannual Comparison of Drought during the Growth Period of Spring Maize

Figure 6 shows the spatial–temporal pattern of the average drought conditions in the early growth stage of spring maize based on the TVDI<sub>N</sub> and in the middle and late growth stages based on the TVDI<sub>E</sub> from 2003 to 2020 in northeast China. Spatially, most of the spring maize area experienced mild drought before and after the seedling stage, and the proportion of moderate drought was relatively low. The drought-affected areas were located in most of Liaoning Province, western Jilin Province, southern eastern Inner Mongolia, and some parts of southwestern Heilongjiang Province. No drought occurred in the eastern Jilin Province, and the influence of spring drought was stronger than that of summer drought before and after the kernel-filling stage in most of Heilongjiang Province. Most of the drought levels in western Liaoning, western Jilin Province, southern Inner Mongolia, and southwestern Heilongjiang Province were mild and moderate. The most serious drought conditions of spring maize occurred from April to May (DOY 105–160) from 2003 to 2020 in the western and southwestern parts of the study area. The drought conditions were weaker from June to July (DOY 161–216), and the drought area decreased, but the spatial distribution of drought differed substantially. Southern Inner Mongolia, southwestern Jilin, and northwest Liaoning are arid areas. Most of Heilongjiang Province and the southeastern Jilin Province experienced no drought. Mild and moderate drought areas are larger in August (DOY 217–240) than in the previous period.

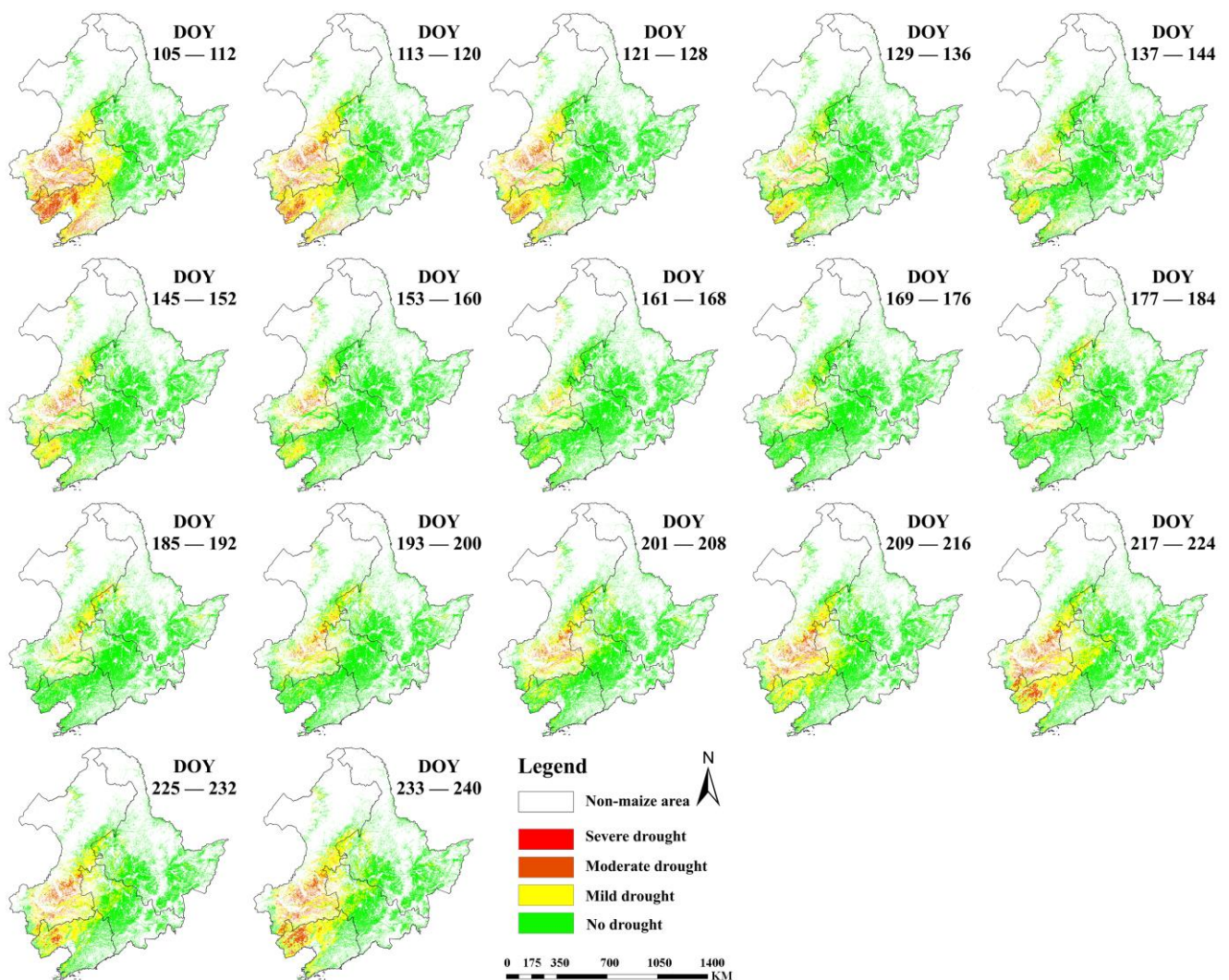


Figure 6. Average drought conditions of spring maize area in northeast China from 2003 to 2020.

The area affected by drought in 2003, 2009, 2013, and 2018 exceeded 30%, and that affected by severe drought accounted for more than 8% (Figure 7).

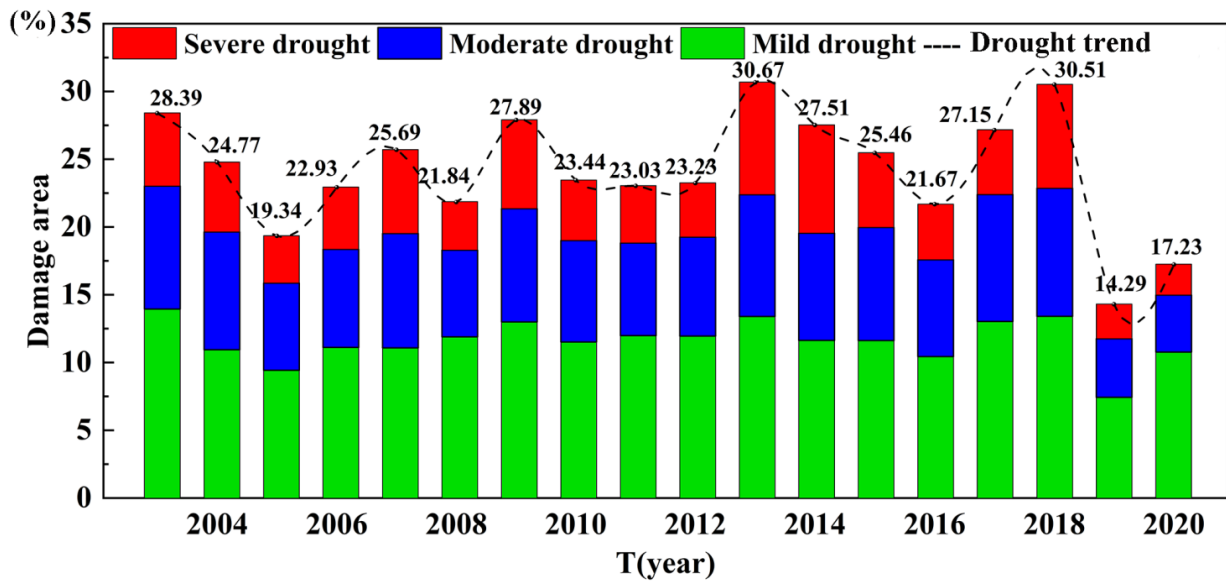


Figure 7. Proportion of area affected annually by different drought levels.

### 3.4. Frequent Drought Periods in the Study Area

Figure 8 shows the percentage of ET0, monthly ET0, percentage of precipitation, and monthly precipitation in northeast China from 1985 to 2020. The precipitation was significantly lower than the ET0 from April to May, limiting the water supply of spring maize and causing drought conditions. The difference between precipitation and ET0 decreased in June, and the drought eased. The precipitation was significantly higher than the ET0 from July to August, and the drought was alleviated in a large area. However, starting in September, the ET0 was significantly higher than the precipitation, and the drought intensified again. The percentage of PRE showed an increasing trend from April to July and a decreasing trend from July to September. The ET0 percentage increased from April to May and decreased from May to September. Frequent droughts occurred in the study area in spring and autumn.

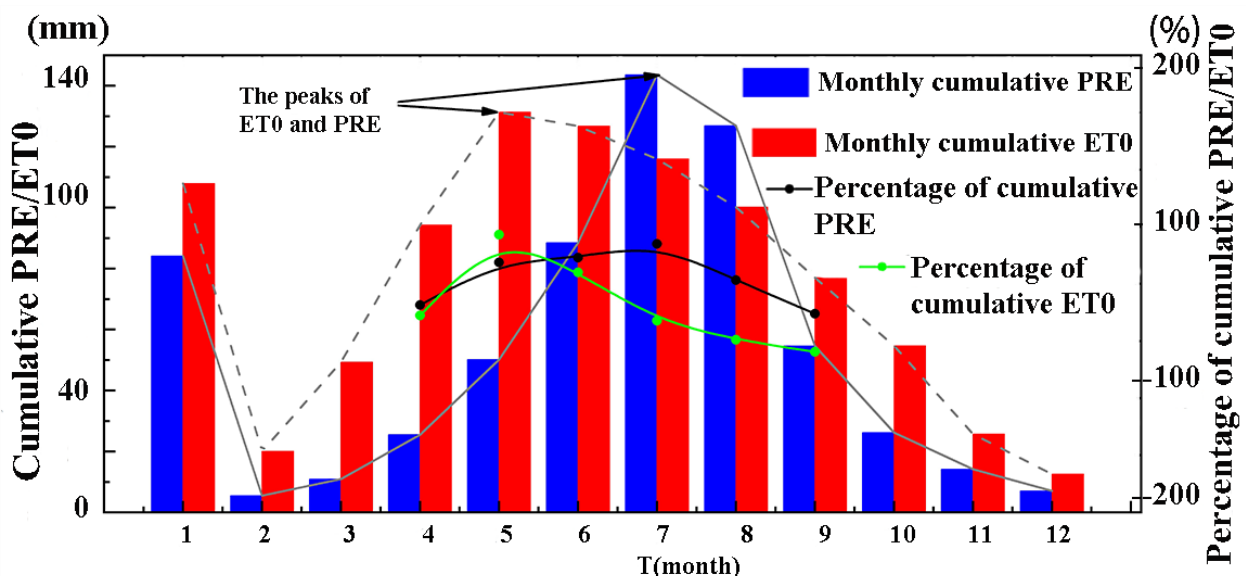


Figure 8. Monthly meteorological indices from 1985 to 2020.

Figure 9 shows the proportion of different drought levels obtained from 8-day TVDI data in northeast China from 2003 to 2020. The area experienced two significant drought events. The first one occurred from April to May. There was very little precipitation, and the glacier meltwater did not reach the cultivated areas, as shown in Figure 9. The vegetation cover was low, or there was bare soil, and the  $ET_0$  was greater than the precipitation, resulting in severe drought events during this period. The second drought occurred in August–September when the maize plants were relatively tall and the water requirement was large. Although rainfall was abundant in this period, the temperature was high, the  $ET_0$  was greater than the precipitation, and the vegetation did not receive sufficient water. The maize was in the jointing–tasseling period from June to July, and the precipitation and temperature were suitable in the study area, providing suitable growing conditions for maize. The drought conditions derived from the TVDI were consistent with those based on the meteorological indices depicted in Figure 8.

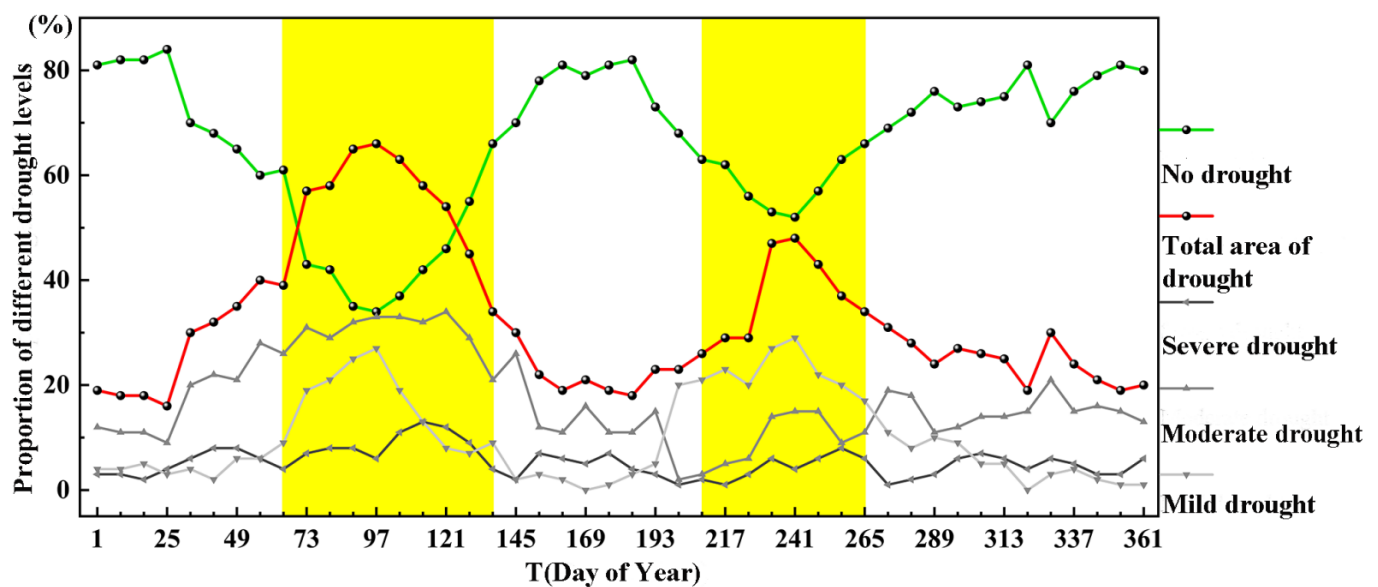


Figure 9. Average drought conditions based on 8-day TVDI data in northeast China from 2003 to 2020.

#### 4. Discussion

##### 4.1. Applicability of TVDI for Monitoring Spring Maize Drought in Northeast China

The difference in the accuracy between the drought conditions obtained from meteorological indices and from remote sensing monitoring was reflected in two aspects [13–15]. First, meteorological monitoring typically uses indices to assess climate change in a specific period to characterise drought conditions. Remote sensing methods have been widely used for drought monitoring, such as the inversion of parameters (e.g., crop canopy parameters). In this study, the accuracy and reliability of the remote sensing-based drought monitoring results were better than those of the meteorological monitoring results. Second, meteorological data are typically point data; thus, interpolation is required to obtain continuous data, and the spatial–temporal resolutions are not sufficiently high. Remote sensing data are raster data with high spatial–temporal resolutions, providing higher accuracy than meteorological data. Numerous experiments have been conducted to verify the feasibility of remote sensing indices for drought monitoring systematically [54–56]. Following previous studies [3,5,7,14,15], we defined the most suitable periods for using the TVDI<sub>N</sub> and TVDI<sub>E</sub> for drought monitoring by calculating the difference in the  $R^2$  for the relationship between the RSM and the TVDI<sub>E</sub> and TVDI<sub>N</sub> (Figure 4). The  $R^2$  of the TVDI<sub>N</sub> (dry edge slope) was higher than that of the TVDI<sub>E</sub> in the seedling–jointing period (DOY 105–150) of spring maize. The fitting performance of the TVDI<sub>E</sub> was significantly higher than that of

the TVDI<sub>E</sub>, and it was more suitable for drought monitoring. The R<sup>2</sup> values of the TVDI<sub>N</sub> and TVDI<sub>E</sub> were the closest during the jointing–kernel-filling period (DOY 150–185), which was regarded as the transition period of TVDI<sub>N</sub> and TVDI<sub>E</sub>. The R<sup>2</sup> of the TVDI<sub>N</sub> (dry edge slope) was lower than that of the TVDI<sub>E</sub> during the kernel-filling period (DOY 185–240). The fitting performance was significantly higher for the TVDI<sub>E</sub> than for the TVDI<sub>N</sub>, making it more suitable for drought monitoring.

The consistency and accuracy of drought monitoring were 84.62% and 78.85% in the early growth stage and 82.69% and 78.85% in the middle and late growth stages, respectively (Table 3). Previous studies [57–59] also observed differences in the sensitive periods when different remote sensing indices were used for drought monitoring, which is consistent with the results of this study. Although previous studies used the same research methods as this study, differences were observed. In previous studies [25,27,40], 16-day products and a TVDI based on different vegetation indices were used for drought monitoring from May to September [57]. These studies showed that the applicability and accuracy of the TVDI based on different parameters did not differ much in the period of low vegetation coverage. However, the applicability and accuracy of the TVDI based on the EVI/LST were higher than those of the TVDI with other parameters in the period of high vegetation coverage. The authors only discussed the sensitivity of the drought indices in different vegetation coverage periods. In contrast, we assessed the sensitive period of TVDI drought monitoring in different developmental stages of spring maize using 8-day remote sensing products. Thus, a more precise period could be defined for TVDI drought monitoring than in previous studies [6,35,37,48], resulting in a more accurate identification of drought periods.

Remote sensing indices used for drought monitoring are affected by the vegetation type and farmland environment, resulting in different levels of applicability. Therefore, the applicability of remote sensing indices should be considered to enable the identification of agricultural drought. Most studies evaluated the correlation between remote sensing indices and RSM [57,58]. Following previous studies [31,39–42], we used the RF model to select suitable indices to describe the relationship between the indices and RSM. The optimal indices were used for drought monitoring in northeast China. The TVDI exhibited higher performance for the drought monitoring of spring maize in northeast China than the other six remote sensing indices (Figure 3).

This study has the following limitations. First, this study focused on the spatial–temporal characteristics of drought in northeast China. However, different agricultural areas are affected by different factors influencing drought, and regional differences exist in the spatial–temporal characteristics of drought. Therefore, a follow-up study will be conducted to analyse more detailed spatial–temporal patterns of drought and influencing factors in different agricultural areas. Second, this study showed that the TVDI was more suitable for the drought monitoring of spring maize in northeast China than other remote sensing indices. This index performed well for drought monitoring in the early (TVDI<sub>N</sub>) and middle and late (TVDI<sub>E</sub>) growth stages of spring maize. However, the meteorological conditions, farmland environment, spring maize varieties, and growth stages differ in different drought conditions. We only considered the farmland environment and development stage. In a follow-up study, we plan to extract VI anomalies in the time series and construct remote sensing indices for different risk areas and different drought periods to perform more accurate real-time and dynamic monitoring of agricultural drought.

#### 4.2. Spatial–Temporal Pattern of Drought in the Study Area

The global surface temperature will continue to rise under the existing greenhouse gas emission scenario, and the water cycle will change, altering the drought pattern and drought risk in China [39]. Drought and waterlogging result in plant water stress. A decreasing drought trend may result in waterlogging. Therefore, understanding the spatial–temporal pattern of drought can prevent or mitigate droughts in areas with frequent droughts and provide information to implement drainage measures to prevent waterlog-

ging in areas with wetting trends. This study used Sen + MK trend analysis to investigate drought trends in the spring maize area in northeast China (Figure 5a). The results showed that the southern, southwestern, and northwestern parts of the study area exhibited an increasing drought trend in the key development stages of spring maize in the past 18 years. Areas with increasing drought trends comprised 37.91% of the area of northeast China. This finding was consistent with that of Wei [60]. Although the drought trend increased in northeast China, differences were observed in different regions. The drought trend increased significantly in the western part of the study area, unlike in the eastern part. It was concluded that the uneven spatial distribution of temperature, precipitation, and climate change in northeast China was the dominant reason.

We examined the change in the slope of the dry and wet edge in the time-series LST-VI feature space to assess the drought trend in northeast China (Figure 5b). The results showed that the dry edge slope showed an upward trend, and the wet edge slope showed a downward trend. Northeast China experienced a trend of increasing drought and decreasing humidity in the past 18 years. The MK mutation test indicated a drought mutation time of nearly 18 years (Figure 5c). The UF and UB curves of the TVDI mean time series intersected in 2005, and the Z-score was 1.96, indicating that the mutation occurred in 2005. Subsequently, the drought showed an upward trend. A significant increase in drought has been observed in northeast China since the 1990s [11,42,48]. Although this study showed a drought trend in northeast China, the trend did not increase significantly. There are two likely reasons. First, different studies analysed different periods. Previous studies focused on the spatial-temporal characteristics of drought in northeast China throughout the year [3,5,61]. In contrast, we focused on the spatial-temporal patterns of drought during the growth period of spring maize. Autumn is also a frequent drought period in this area [42]. The precipitation is significantly lower in autumn. Many storms occur in the monsoon season, resulting in the rapid evaporation of soil moisture and drought. The crops are harvested in autumn, leading to low vegetation coverage and less soil moisture retention. Remote sensing inversion methods for soil moisture and canopy status have been used to assess drought.

The second reason is the difference in the study area. Previous studies focused on larger regions or agricultural areas in northeast China [3–6,8,9,40], whereas this study considered spring maize planting areas. Inner Mongolia in the western part of the study area is characterised by sandy soil, uneven precipitation, and high altitude (Figure 1f–h). It experiences frequent drought, but no maize is planted in this area (Figure 1a). Therefore, this study did not consider Inner Mongolia's drought trend, leading to different results compared to previous studies. Our conclusions regarding the spatial-temporal trend of drought in northeast China are reasonable considering these factors.

In addition, previous studies also observed differences in the spatial-temporal drought trend in northeast China [21,23–25,37,39]. We found that drought before and after the seedling period in northeast China occurred predominantly in the western Liaoning Province, western Jilin Province, southern Inner Mongolia, and southwestern Heilongjiang Province. Drought was less common before and after the jointing period, when most of the study area experienced no drought. Drought before and after the filling period occurred primarily in western Liaoning, western Jilin Province, southern Inner Mongolia, and southwestern Heilongjiang Province. It is assumed that these spatial differences in drought are due to the farmland properties, soil type, topography, and climate change, which contributed to the region's susceptibility to drought. The soil texture in the drought-prone areas was predominantly loam and sand, and the slope was relatively steep, making the region prone to soil erosion. In addition, the spring temperature in the region rises rapidly, but the precipitation is insufficient, and none of the spring glacier meltwater in the Changbai Mountains and the Greater Khingan Mountains reach the region. The combined effects of these conditions caused differences in the soil moisture in the region, resulting in large areas of spring drought. Northeast China experienced extensive periods of rain and heat, easing the drought extent and intensity in the region.

Spring warming occurs fast in northeast China, but the precipitation amount is generally low [11,12]. Summer is characterised by high heat and precipitation. The precipitation amount decreases in autumn, but the temperature does not decrease significantly [44]. We calculated the percentage of ET<sub>0</sub> and precipitation and the monthly scale ET<sub>0</sub> and precipitation [43] (Figure 8). The results showed that the precipitation in April and May was significantly lower than the ET<sub>0</sub>, indicating low RSM and vegetation water stress, resulting in drought. The difference between the TVDI<sub>N</sub> and TVDI<sub>E</sub> was the lowest in June reduced; the RSM increased, and the drought eased. The precipitation was significantly higher than the ET<sub>0</sub> from July to August, and the drought was alleviated in a large area. However, the ET<sub>0</sub> was significantly higher than the precipitation starting in September, and the drought intensified again. However, spring maize was in the milk period at this time, and the severe drought did not affect the yield. This result was consistent with the drought trend obtained from the optimal remote sensing index (Figure 9). Therefore, the trend of climatic factors changed the drought conditions. In general, spring and summer are drought-prone periods for spring maize planting areas, and the western, southern, and southwestern parts of northeast China are drought-prone areas. Irrigation measures should be implemented in these periods and areas to prevent a reduction in spring maize yield caused by drought. In addition to focusing on the increasing drought trend in the Liaohe Plain, we should also consider the possibility of waterlogging in the Sanjiang Plain and Songnen Plain.

## 5. Conclusions

The accuracy improvement of agricultural drought monitoring and the applicability of remote sensing indices have become hot research topics. This study examined the applicability of seven commonly used remote sensing indices for the drought monitoring of spring maize in northeast China using the RF model. The results showed that all seven remote sensing indices were suitable for drought monitoring in the study area, but the TVDI exhibited the best performance. The TVDI<sub>N</sub> had high sensitivity and accuracy in the early stage of spring maize development, whereas the TVDI<sub>E</sub> performed better in the middle and late stages. The spatial–temporal patterns of drought in northeast China were investigated using the TVDI<sub>N</sub> and TVDI<sub>E</sub> drought-monitoring indicators. The most severe drought occurred from April to May, which was followed by a weakening of the drought from June to July, with large regional differences. The severe drought area increased again in August. The dominant drought-affected areas included most of Liaoning Province, western Jilin Province, the southern East Fourth League of Inner Mongolia, and some parts of southwestern Heilongjiang Province. This study identified spatial–temporal differences in precipitation and ET<sub>0</sub> as the main causes of drought in the study area.

**Author Contributions:** Data curation, Y.W. (Yihao Wang) and Y.W. (Yongfeng Wu); Formal analysis, Y.W. (Yihao Wang), Y.W. (Yongfeng Wu) and L.J.; Methodology, Y.W. (Yihao Wang); Project administration, Y.W. (Yongfeng Wu); Software, Y.W. (Yihao Wang), Y.W. (Yongfeng Wu) and J.Z.; Writing—original draft, Y.W. (Yihao Wang); Writing—review and editing, Y.W. (Yongfeng Wu) and L.M. All authors have read and agreed to the published version of the manuscript.

**Funding:** This research was funded by the National Key Technologies Research and Development Program of China, grant number 2017YFD0300402-2.

**Data Availability Statement:** Data is privacy restrictions, please contact the corresponding author.

**Acknowledgments:** This work were supported by MODIS and Sentinel-2 data, which provided by NASA and ESA. As the same time, I sincerely appreciate to Haixv Zhang, thanks for your efforts to revise my paper, wish you a happy Qixi Festival.

**Conflicts of Interest:** The authors declare no conflict of interest.

## References

- Kelley, C.P.; Mohtadi, S.; Cane, M.A.; Seager, R.; Kushnir, Y. Climate change in the Fertile Crescent and implications of the recent Syrian drought. *Proc. Natl. Acad. Sci. USA* **2015**, *112*, 3241–3246. [\[CrossRef\]](#)
- Du, Y.; Feng, G.; Li, Z.; Peng, X.; Zhu, J.; Ren, Z. Effects of External Digital Elevation Model Inaccuracy on StaMPS-PS Processing: A Case Study in Shenzhen, China. *J. Remote Sens.* **2017**, *9*, 1115. [\[CrossRef\]](#)
- Dang, Y.; Qin, L.; Huang, L.; Wang, J.; Li, B.; He, H. Water footprint of rain-fed maize in different growth stages and associated climatic driving forces in Northeast China. *Agric. Water Manag.* **2022**, *263*, 107463. [\[CrossRef\]](#)
- Sun, P.; Ma, Z.; Zhang, Q.; Singh, V.P.; Xu, C.-Y. Modified drought severity index: Model improvement and its application in drought monitoring in China. *J. Hydrol.* **2022**, *612*, 128097. [\[CrossRef\]](#)
- Du, C.; Chen, J.; Nie, T.; Dai, C. Spatial-temporal changes in meteorological and agricultural droughts in Northeast China: Change patterns, response relationships and causes. *Nat. Hazards* **2021**, *110*, 155–173. [\[CrossRef\]](#)
- Zhang, Q.; Shi, R.; Xu, C.-Y.; Sun, P.; Yu, H.; Zhao, J. Multisource data-based integrated drought monitoring index: Model development and application. *J. Hydrol.* **2022**, *615*, 128644. [\[CrossRef\]](#)
- Wang, Q.; Huo, Z.; Zhang, L.; Wang, J.; Zhao, Y. Impact of saline water irrigation on water use efficiency and soil salt accumulation for spring maize in arid regions of China. *Agric. Water Manag.* **2016**, *163*, 125–138. [\[CrossRef\]](#)
- Feng, G.Z.; He, X.L.; Coulter, J.A.; Chen, Y.L.; Gao, Q.; Mi, G.H. Effect of limiting vertical root growth on maize yield and nitrate migration in clay and sandy soils in Northeast China. *Soil Tillage Res.* **2019**, *195*, 104407. [\[CrossRef\]](#)
- Ji, Y.; Zhou, G.; He, Q.; Wang, L. The effect of climate change on spring maize (*Zea mays* L.) suitability across China. *Sustainability* **2018**, *10*, 3804. [\[CrossRef\]](#)
- Wang, Y.; Meng, L.; Liu, H.; Luo, C.; Bao, Y.; Qi, B.; Zhang, X. Construction and Assessment of a Drought-Monitoring Index Based on Multi-Source Data Using a Bias-Corrected Random Forest (BCRF) Model. *Remote Sens.* **2023**, *15*, 2477. [\[CrossRef\]](#)
- Jürgens, C. The modified normalization difference vegetation index (mNDVI): A new index to determine frost damages in agriculture based on Landsat TM data. *Int. J. Remote Sens.* **1997**, *18*, 3583–3594. [\[CrossRef\]](#)
- Kent, C.; Pope, E.; Dunstone, N.; Scaife, A.A.; Tian, Z.; Clark, R.; Zhang, L.; Davie, J.; Lewis, K. Maize Drought Hazard in the Northeast Farming Region of China: Unprecedented Events in the Current Climate. *J. Appl. Meteorol. Clim.* **2019**, *58*, 2247–2258. [\[CrossRef\]](#)
- Zhong, R.; Zhao, T.; Chen, X.; Jin, H. Monitoring drought in ungauged areas using satellite altimetry: The Standardized River Stage Index. *J. Hydrol.* **2022**, *612*, 128308. [\[CrossRef\]](#)
- Kourouma, J.M.; Eze, E.; Negash, E.; Phiri, D.; Vinya, R.; Girma, A.; Zenebe, A. Assessing the spatio-temporal variability of NDVI and VCI as indices of crops productivity in Ethiopia: A remote sensing approach. *Geomat. Nat. Hazards Risk* **2021**, *12*, 2880–2903. [\[CrossRef\]](#)
- Zhao, Z.; Wang, H.; Qin, D.; Wang, C. Large-scale monitoring of soil moisture using Temperature Vegetation Quantitative Index (TVQI) and exponential filtering: A case study in Beijing. *Agric. Water Manag.* **2021**, *252*, 106896. [\[CrossRef\]](#)
- Tagesson, T.; Horion, S.; Nieto, H.; Fornies, V.Z.; González, G.M.; Bulgin, C.; Ghent, D.; Fensholt, R. Disaggregation of SMOS soil moisture over West Africa using the Temperature and Vegetation Dryness Index based on SEVIRI land surface parameters. *Remote Sens. Environ.* **2018**, *206*, 424–441. [\[CrossRef\]](#)
- Mu, S.; Yang, G.; Xu, X.; Wan, R.; Li, B. Assessing the inundation dynamics and its impacts on habitat suitability in Poyang Lake based on integrating Landsat and MODIS observations. *Sci. Total Environ.* **2022**, *834*, 154936. [\[CrossRef\]](#)
- Wan, W.; Liu, Z.; Li, K.; Wang, G.; Wu, H.; Wang, Q. Drought monitoring of the maize planting areas in Northeast and North China Plain. *Agric. Water Manag.* **2021**, *245*, 106636. [\[CrossRef\]](#)
- Lv, S.; Li, X.; Wang, R.; Wang, Y.; Dong, Z.; Zhou, T.; Liu, Y.; Lin, K.; Liu, L. Autochthonous sources and drought conditions drive anomalous oxygen-consuming pollution increase in a sluice-controlled reservoir in eastern China. *Sci. Total Environ.* **2022**, *841*, 156739. [\[CrossRef\]](#)
- Tucker, C.J.; Justice, C.O.; Prince, S.D. Monitoring the grasslands of the Sahel 1984–1985. *Int. J. Remote Sens.* **1986**, *7*, 1571–1581. [\[CrossRef\]](#)
- Kogan, F.N. Remote sensing of weather impacts on vegetation in non-homogeneous areas. *Int. J. Remote Sens.* **1990**, *11*, 1405–1419. [\[CrossRef\]](#)
- Qing Liu, H.; Huete, A. A feedback based modification of the NDVI to minimize canopy background and atmospheric noise. *IEEE Trans. Geosci. Remote Sens.* **1995**, *33*, 457–465. [\[CrossRef\]](#)
- Kogan, F. Application of vegetation index and brightness temperature for drought detection. *Adv. Space Res.* **1995**, *15*, 91–100. [\[CrossRef\]](#)
- Carlson, T.N.; Gillies, R.R.; Perry, E.M. A method to make use of thermal infrared temperature and NDVI measurements to infer surface soil water content and fractional vegetation cover. *Remote Sens. Rev.* **1994**, *9*, 161–173. [\[CrossRef\]](#)
- Sandholt, I.; Rasmussen, K.; Andersen, J. A simple interpretation of the surface temperature/vegetation index space for assessment of surface moisture status. *Remote Sens. Environ.* **2002**, *79*, 213–224. [\[CrossRef\]](#)
- Abbas, S.; Nichol, J.E.; Qamer, F.M.; Xu, J. Characterization of Drought Development through Remote Sensing: A Case Study in Central Yunnan, China. *Remote Sens.* **2014**, *6*, 4998–5018. [\[CrossRef\]](#)
- Idso, S.B.; Jackson, R.D.; Pinter, P.J., Jr.; Reginato, R.J.; Hatfield, J.L. Normalizing the stress-degree-day parameter for environmental variability. *Agric. Meteorol.* **1981**, *24*, 45–55. [\[CrossRef\]](#)

28. Moran, M.S.; Clarke, T.R.; Inoue, Y.; Vidal, A. Estimating crop water deficit using the relation between surface-air temperature and spectral vegetation index. *Remote Sens. Environ.* **1994**, *49*, 246–263. [[CrossRef](#)]
29. Wan, W.; Liu, Z.; Li, J.; Xu, J.; Wu, H.; Xu, Z. Spatiotemporal patterns of maize drought stress and their effects on biomass in the Northeast and North China Plain from 2000 to 2019. *Agric. For. Meteorol.* **2022**, *315*, 108821. [[CrossRef](#)]
30. Peng, J.; Loew, A.; Zhang, S.; Wang, J.; Niesel, J. Spatial Downscaling of Satellite Soil Moisture Data Using a Vegetation Temperature Condition Index. *IEEE Trans. Geosci. Remote Sens.* **2016**, *54*, 558–566. [[CrossRef](#)]
31. Wang, R.; Gamon, J.A.; Emmerton, C.A.; Springer, K.R.; Yu, R.; Hmimina, G. Detecting intra- and inter-annual variability in gross primary productivity of a North American grassland using MODIS MAIAC data. *Agric. For. Meteorol.* **2020**, *281*, 107859. [[CrossRef](#)]
32. Sun, B.; Qian, J.; Chen, X.; Zhou, Q. Comparison and Evaluation of Remote Sensing Indices for Agricultural Drought Monitoring over Kazakhstan. *Int. Arch. Photogramm. Remote Sens. Spat. Inf. Sci.* **2020**, *43*, 899–903. [[CrossRef](#)]
33. Zhao, H.; Li, Y.; Chen, X.; Wang, H.; Yao, N.; Liu, F. Monitoring monthly soil moisture conditions in China with temperature vegetation dryness indexes based on an enhanced vegetation index and normalized difference vegetation index. *Theor. Appl. Clim.* **2020**, *143*, 159–176. [[CrossRef](#)]
34. Zhang, S.; Chen, X.; Jia, S.; Liang, A.; Zhang, X.; Yang, X.; Wei, S.; Sun, B.; Huang, D.; Zhou, G. The potential mechanism of long-term conservation tillage effects on maize yield in the black soil of Northeast China. *Soil Tillage Res.* **2015**, *154*, 84–90. [[CrossRef](#)]
35. Heim, R.R., Jr. A Review of Twentieth-Century Drought Indices Used in the United States. *Bull. Am. Meteorol. Soc.* **2002**, *83*, 1149–1166. [[CrossRef](#)]
36. Li, S.; Xu, Q.; Yi, J.; Liu, J. Construction and application of comprehensive drought monitoring model considering the influence of terrain factors: A case study of southwest Yunnan, China. *Environ. Sci. Pollut. Res.* **2022**, *29*, 72655–72669. [[CrossRef](#)] [[PubMed](#)]
37. Trisasonko, B.H.; Panuju, D.R.; Shiddiq, D.; Iman, L.O.S.; Sholihah, R.I.; Kusdaryanto, S. Constraints of VSWI in the Estimation of Drought Extent Using Landsat Data: A Case of Tuban, Indonesia. *Procedia Environ. Sci.* **2015**, *24*, 25–28. [[CrossRef](#)]
38. Kleshchenko, A.D.; Asmus, V.V.; Strashnaya, A.I.; Krovotyntsev, V.A.; Virchenko, O.V.; Savitskaya, O.V.; Bereza, O.V.; Vasilenko, E.V.; Sukhareva, V.V.; Morgunov, Y.A.; et al. Drought Monitoring Based on Ground and Satellite Data. *Russ. Meteorol. Hydrol.* **2019**, *44*, 772–781. [[CrossRef](#)]
39. Fu, R.; Chen, R.; Wang, C.; Chen, X.; Gu, H.; Wang, C.; Xu, B.; Liu, G.; Yin, G. Generating High-Resolution and Long-Term SPEI Dataset over Southwest China through Downscaling EEAD Product by Machine Learning. *Remote Sens.* **2022**, *14*, 1662. [[CrossRef](#)]
40. Liu, L.; Liao, J.; Chen, X.; Zhou, G.; Su, Y.; Xiang, Z.; Wang, Z.; Liu, X.; Li, Y.; Wu, J.; et al. The Microwave Temperature Vegetation Drought Index(MTVDI) based on AMSR-E, brightness temperatures for long-term drought asses-sment across China(2003–2010). *J. Remote Sens. Environ.* **2017**, *199*, 302–320. [[CrossRef](#)]
41. Guo, P.-T.; Li, M.-F.; Luo, W.; Tang, Q.-F.; Liu, Z.-W.; Lin, Z.-M. Digital mapping of soil organic matter for rubber plantation at regional scale: An application of random forest plus residuals kriging approach. *Geoderma* **2015**, *237–238*, 49–59. [[CrossRef](#)]
42. Guo, H.; Li, M.; Nzabarinda, V.; Bao, A.; Meng, X.; Zhu, L.; De Maeyer, P. Assessment of Three Long-Term Satellite-Based Precipitation Estimates against Ground Observations for Drought Characterization in Northwestern China. *Remote Sens.* **2022**, *14*, 828. [[CrossRef](#)]
43. Zhang, Q.; Hu, Z. Assessment of drought during corn growing season in Northeast China. *Theor. Appl. Clim.* **2018**, *133*, 1315–1321. [[CrossRef](#)]
44. Zhu, L.; Cooper, D.J.; Han, S.; Yang, J.; Zhang, Y.; Li, Z.; Zhao, H.; Wang, X. Influence of the atlantic multidecadal oscillation on drought in northern Daxing'an mountains, Northeast China. *Catena* **2020**, *198*, 105017. [[CrossRef](#)]
45. Duan, Y.; Zhong, J.; Shuai, G.; Zhu, S.; Gu, X. Time-Scale Transferring Deep Convolutional Neural Network for Mapping Early Rice. In *IGARSS 2018—2018 IEEE International Geoscience and Remote Sensing Symposium*; Valencia, C., Ed.; IEEE: Piscataway, NJ, USA, 2018; pp. 1136–1139. [[CrossRef](#)]
46. Schepaschenko, D.; See, L.; Lesiv, M.; McCallum, I.; Fritz, S.; Salk, C.; Moltchanova, E.; Perger, C.; Shchepashchenko, M.; Shvidenko, A.; et al. Development of a global hybrid forest mask through the synergy of remote sensing, crowdsourcing and FAO statistics. *J. Remote Sens. Environ.* **2015**, *162*, 208–220. [[CrossRef](#)]
47. Luo, C.; Zhang, X.; Meng, X.; Zhu, H.; Ni, C.; Chen, M.; Liu, H. Regional mapping of soil organic matter content using multitemporal synthetic Landsat 8 images in Google Earth Engine. *Catena* **2022**, *209*, 105842. [[CrossRef](#)]
48. Javed, T.; Li, Y.; Rashid, S.; Li, F.; Hu, Q.; Feng, H.; Chen, X.; Ahmad, S.; Liu, F.; Pulatov, B. Performance and relationship of four different agricultural drought indices for drought monitoring in China's mainland using remote sensing data. *Sci. Total Environ.* **2020**, *759*, 143530. [[CrossRef](#)]
49. Wen, Z.; Shen, J.; Blackwell, M.; Li, H.; Zhao, B.; Yuan, H. Combined Applications of Nitrogen and Phosphorus Fertilizers with Manure Increase Maize Yield and Nutrient Uptake via Stimulating Root Growth in a Long-Term Experiment. *Pedosphere* **2016**, *26*, 62–73. [[CrossRef](#)]
50. Ma, M.; Ren, L.; Singh, V.P.; Tu, X.; Jiang, S.; Liu, Y. Evaluation and application of the SPDI-JDI for droughts in Texas, USA. *J. Hydrol.* **2015**, *521*, 34–35. [[CrossRef](#)]
51. Rek, Z.; Sarler, B. Engineering analysis with boundary elements the method of fundamental solutions for the Stokes flow with the subdomain technique. *Eng. Anal. Bound. Elem.* **2021**, *128*, 80–89. [[CrossRef](#)]
52. Mann, H.B. Nonparametric tests against trend. *Econometrica* **1945**, *13*, 245–259. [[CrossRef](#)]

53. Vicente-Serrano, S.M.; Beguería, S.; López-Moreno, J.I. A multiscale drought index sensitive to global warming: The standardized precipitation evapotranspiration index. *J. Clim.* **2010**, *23*, 1696–1718. [[CrossRef](#)]
54. Xin, J.; Tian, G.; Liu, Q.; Chen, L. Combining vegetation index and remotely sensed temperature for estimation of soil moisture in China. *Int. J. Remote Sens.* **2006**, *27*, 2071–2075. [[CrossRef](#)]
55. Ciężkowski, W.; Szporak-Wasilewska, S.; Kleniewska, M.; Józwiak, J.; Gnatowski, T.; Dąbrowski, P.; Góraj, M.; Szatyłowicz, J.; Ignar, S.; Chormański, J. Remotely Sensed Land Surface Temperature-Based Water Stress Index for Wetland Habitats. *Remote Sens.* **2020**, *12*, 631. [[CrossRef](#)]
56. Zhang, Y.; Huang, S.; Huang, Q.; Leng, G.; Wang, H.; Wang, L. Assessment of drought evolution characteristics based on a nonparametric and trivariate integrated drought index—Science Direct. *J. Hydrol.* **2019**, *579*, 124230. [[CrossRef](#)]
57. He, D.; Yi, G.; Zhang, T.; Miao, J.; Li, J.; Bie, X. Temporal and Spatial Characteristics of EVI and Its Response to Climatic Factors in Recent 16 years Based on Grey Relational Analysis in Inner Mongolia Autonomous Region, China. *Remote Sens.* **2018**, *10*, 961. [[CrossRef](#)]
58. Testa, S.; Soudani, K.; Boschetti, L.; Mondino, E.B. MODIS-derived EVI, NDVI and WDRVI time series to estimate phenological metrics in French deciduous forests. *Int. J. Appl. Earth Obs. Geoinf.* **2018**, *64*, 132–144. [[CrossRef](#)]
59. Du, L.; Song, N.; Liu, K.; Hou, J.; Hu, Y.; Zhu, Y.; Wang, X.; Wang, L.; Guo, Y. Comparison of Two Simulation Methods of the Temperature Vegetation Dryness Index (TVDI) for Drought Monitoring in Semi-Arid Regions of China. *Remote Sens.* **2017**, *9*, 177. [[CrossRef](#)]
60. Wan, W.; Liu, Z.; Li, B.; Fang, H.; Wu, H.; Yang, H. Evaluating soil erosion by introducing crop residue cover and anthropogenic disturbance intensity into cropland C-factor calculation: Novel estimations from a cropland-dominant region of Northeast China. *Soil Tillage Res.* **2022**, *219*, 105343. [[CrossRef](#)]
61. Qin, Y.; Xiao, X.; Wigneron, J.-P.; Ciais, P.; Canadell, J.G.; Brandt, M.; Li, X.; Fan, L.; Wu, X.; Tang, H.; et al. Large loss and rapid recovery of vegetation cover and aboveground biomass over forest areas in Australia during 2019–2020. *Remote Sens. Environ.* **2022**, *278*, 113087. [[CrossRef](#)]

**Disclaimer/Publisher’s Note:** The statements, opinions and data contained in all publications are solely those of the individual author(s) and contributor(s) and not of MDPI and/or the editor(s). MDPI and/or the editor(s) disclaim responsibility for any injury to people or property resulting from any ideas, methods, instructions or products referred to in the content.